2023 IEEE International Conference on Robotics and Automation (ICRA 2023)
May 29 - June 2, 2023. London, UK

On the Learned Balance Manifold of Underactuated Balance Robots

Feng Han and Jingang Yi

Abstract— **Tracking control of underactuated balance robots needs to estimate balance profiles, that is, balance equilibrium manifold (BEM) of the unactuated subsystems. We present a learning-based approach to obtain the balance manifold for underactuated balance robots. We first establish the relationship between the BEM and the zero dynamics of the underactuated balance robots. The analysis shows that the BEM is a close approximation of the equilibria of the zero dynamics under perfectly tracking control. A Gaussian process learning-based method is proposed to estimate and obtain the BEM and zero dynamics, avoiding the direct inversion of the physics-based robot dynamic model. We demonstrate the analysis and applications experimentally on a rotary inverted pendulum and a bipedal robot.**

I. Introduction

Motion control of underactuated balance robots requires trajectory tracking of an actuated subsystem and balance of an unactuated subsystem [1]–[3]. For example, trajectory tracking of the actuated base link of a rotary inverted pendulum requires the unactuated pendulum link to be balanced around the upright position [2]. Another example of underactuated balance robots is the autonomous bicycle (i.e., bikebot) [4], [5]. The output trajectory is the bikebot position, while the roll dynamics is unactuated that needs to be balanced. The desired trajectory of the actuated subsystem is given but the required balance profile, or balance manifold, for the unactuated subsystem needs to be estimated in real-time. Due to the non-minimum phase property of the unactuated subsystem, obtaining the balance manifold requires inverting the unstable dynamics and often results in non-causal control design [6].

Robot controllers need to fulfill both the trajectory tracking task and balance task. The stability and balance of the unactuated subsystem determine the robot output tracking performance. For instance, a large pitch motion of a torso or trunk causes the bipedal walker unstable and diverging from desired gait [7], [8]. One critical challenge in the control of underactuated balance robots is to determine the balance manifold, that is, the desired profile of the unactuated subsystem for a given trajectory. In [1], the researcher presented the external and internal convertible (EIC)-based control framework, and balance equilibrium manifold (BEM) is introduced to account for the coupling effects between the actuated and unactuated subsystems [1], [9]. The BEM defines the instantaneous equilibrium of the unactuated subsystems given the current tracking performance. The closed-loop system is shown to be exponentially stable under EIC-based control. Although serving as the desired balance manifold, the BEM does not satisfy the system dynamics. Instead, zero dynamics capture the motion of the unactuated subsystem when output follows the given trajectory or the designed virtual constraints [10]. For periodical motion, the orbital stabilization method can be used for bipedal walker gait design [11], [12]. For underactuated balance robots, analysis of zero dynamics helps reveal the ultimate response of the unactuated subsystem. For example, the existence of the stable, periodic solutions of zero dynamics of a bipedal walker indicates the feasibility of gait design, which is usually formulated as an optimization problem [13]–[15].

All of the above-discussed works are based on known robot dynamic models. For high-dimensional robotic systems, it is challenging to obtain an accurate physical dynamic model, and this is particularly difficult when robots interact with dynamic and complex environments. Machine learning techniques, on the other hand, provide an alternative means to construct data-driven dynamic models and control [16], [17]. In [2], [3], Gaussian process (GP) regression models were used to obtain the robot dynamics of underactuated balance robots. The BEMs were estimated by direct inversion of the GP model in the design. However, no relationship was discussed between the learned balance manifold and the zero dynamics of robotic systems [2], [3]. In [18], the researchers showed that the zero dynamics of bipedal walkers are equivalent to the learned GP dynamics model (GPDM). The GPDM is obtained by using training data set that are generated under perfect tracking conditions [18]. However, it is unclear how to obtain BEM from the GPDM and to further build a relationship with the zero dynamics.

We present a learning-based balance manifold estimation method for underactuated balance robots. We first show that the BEM is closely related to the zero dynamics of underactuated balance robots. One attractive feature by revealing this relationship is to understand the behavior and property of the zero dynamics without solving the differential equations. We propose to use a GP model to simultaneously capture the unactuated system dynamics and calculate the BEM. Using the GP model, we avoid inversion strategies to obtain the balance manifold and therefore, approximate the dynamic behavior of the zero dynamics. We demonstrate the analysis and BEM calculation with applications through two experimental platforms: a rotary inverted (Furata) pendulum and a biped robotic walker.

The main contributions of this work are twofold. First, the

This work was partially supported by the US National Science Foundation under award CNS-1932370.

F. Han and J. Yi are with the Department of Mechanical and Aerospace Engineering, Rutgers University, Piscataway, NJ 08854 USA (e-mail: fh233@scarletmail.rutgers.edu; jgyi@rutgers.edu).

analytical relationship between the zero dynamics and the BEM of the underactuated balance robots is new. Second, we build a machine learning method to estimate the BEM and therefore, provide a connection between the learning-based and physics-based robot dynamics. This is particularly useful for constructing data-driven robot dynamics and control, when physical models are unavailable. The results further show the complementary properties among the zero dynamics, the BEM and GPDM for underactuated balance robots.

II. Underactuated Balance Robots and Problem Statement

Fig. 1 shows two examples of underactuated balance robots. The rotary inverted pendulum shown in Fig. 1(a) has two degrees of freedom (DOFs): the base link joint α (actuated) and the inverted pendulum link joint θ (unactuated). The bipedal robotic walker shown in Fig. 1(b) has five DOFs: torso joint (q_1) is unactuated, and hip (q_2 and q_4) and knee (q_3 and q_5) joints are actuated. The knees joints are actuated through chains with two motors installed at the hip position.

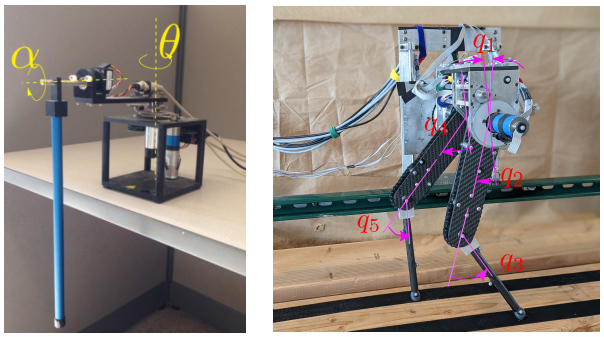

(a) (b)

Fig. 1. (a) A Furuta pendulum. The base link angle α is actuated and the pendulum link θ is unactuated. (b) A bipedal robot.

We consider a general underactuated balance robot with n DOFs, $n \in \mathbb{N}$, and the generalized coordinates are denoted as $\boldsymbol{q} = [q_1 \cdots q_n]^T$. For simplicity and without loss of generality, we assume that the number of unactuated coordinate is one, which appears in most underactuated robots system, such as cart-pendulum [19], bipedal walker [7], and autonomous bikebot [4]. Then, the generalized coordinates are partitioned as $\boldsymbol{q} = [\boldsymbol{q}_a^T \ q_u]^T$, with actuated joint coordinate vector $\boldsymbol{q}_a \in \mathbb{R}^{n-1}$ and unactuated joint $q_u \in \mathbb{R}$. The robot dynamics are written into a standard form as

$$\mathcal{S} : \boldsymbol{D}(\boldsymbol{q})\ddot{\boldsymbol{q}} + \boldsymbol{C}(\boldsymbol{q}, \dot{\boldsymbol{q}})\dot{\boldsymbol{q}} + \boldsymbol{G}(\boldsymbol{q}) = \boldsymbol{B}\boldsymbol{u}, \tag{1}$$

where $\boldsymbol{D}(\boldsymbol{q})$, $\boldsymbol{C}(\boldsymbol{q}, \dot{\boldsymbol{q}})$ and $\boldsymbol{G}(\boldsymbol{q})$ are the inertia, Coriolis and gravitational matrices, respectively. $\boldsymbol{u} \in \mathbb{R}^{n-1}$ is the control torque vector, and the input matrix $\boldsymbol{B} = \text{diag}(\boldsymbol{I}_{n-1}, 0) \in \mathbb{R}^{n\times(n-1)}$ is constant, where $\boldsymbol{I}_{n-1}$ denotes the identity matrix of dimension $n-1$. Note that for robot dynamics that experiences impact and other discontinuous effects (e.g., bipedal walkers), model (1) is still applied to the continuous moving phase (e.g., single- or double-stance phases).

The dynamic model (1) is then written into the form

$$\mathcal{S}_a : \boldsymbol{D}_{aa}\ddot{\boldsymbol{q}}_a + \boldsymbol{D}_{au}\ddot{q}_u + \boldsymbol{C}_{aa}\dot{\boldsymbol{q}}_a + \boldsymbol{C}_{au}\dot{q}_u + \boldsymbol{G}_a = \boldsymbol{u}, \tag{2a}$$

$$\mathcal{S}_u : \boldsymbol{D}_{ua}\ddot{\boldsymbol{q}}_a + D_{uu}\ddot{q}_u + \boldsymbol{C}_{ua}\dot{\boldsymbol{q}}_a + C_{uu}\dot{q}_u + G_u = 0, \tag{2b}$$

where the subscripts aa (uu) and ua/au indicate the variables related to the actuated (unactuated) joints and coupling effects, respectively. From now on, the dependence of matrices $\boldsymbol{D}$, $\boldsymbol{C}$, and $\boldsymbol{G}$ on $\boldsymbol{q}$ and $\dot{\boldsymbol{q}}$ is dropped for presentation clarity. By the robot dynamics properties [20], we have $\boldsymbol{D}_{au} = \boldsymbol{D}_{au}^T$. Since the ith principal moment of inertia does not depend on the ith motion coordinate, we obtain $\frac{\partial D_{ii}}{\partial q_i} = 0$, $i = 1, \cdots, n$, where D_{ii} denotes the ith diagonal element of $\boldsymbol{D}$. The (i,j)th element of matrix $\boldsymbol{C}$ is constructed as $C_{ij} = \sum_{k=1}^{n} c_{ijk}\dot{q}_k$, where c_{ijk} is the Christoffel symbols [20].

Letting $\boldsymbol{q}_a^d$ denote desired actuated trajectory, the output of the robotic system (1) is $\boldsymbol{y} = \boldsymbol{q}_a - \boldsymbol{q}_a^d$. Output $\boldsymbol{y}$ can also be viewed as a virtual constraint. To drive the output to zero, the feedback linearization controller is designed as

$$\boldsymbol{u} = \boldsymbol{D}_{aa}\boldsymbol{v}_a^{\text{ext}} + \boldsymbol{D}_{au}\ddot{q}_u + \boldsymbol{C}_{aa}\dot{\boldsymbol{q}}_a + \boldsymbol{C}_{au}\dot{q}_u + \boldsymbol{G}_a, \tag{3}$$

where $\boldsymbol{v}_a^{\text{ext}}$ is the auxiliary control such that the closed-loop system becomes $\ddot{\boldsymbol{q}}_a = \boldsymbol{v}_a$. Under a proper design of $\boldsymbol{v}_a^{\text{ext}}$, we obtain $\boldsymbol{y} \to \boldsymbol{0}$ exponentially. The leftover of the system dynamics is the zero dynamics. The zero dynamics (in term of q_u) is given as

$$\mathcal{S}_0 : D_{uu}\ddot{q}_u + \boldsymbol{D}_{ua}\ddot{\boldsymbol{q}}_a^d + C_{uu}\dot{q}_u + \boldsymbol{C}_{ua}\dot{\boldsymbol{q}}_a^d + G_u = 0. \tag{4}$$

The profile of the unactuated joint motion from zero dynamics under $\boldsymbol{q}_a = \boldsymbol{q}_a^d$ is denoted as q_u^d. For presentation convenience, from (4), we define function

$$\Gamma(q_u; \boldsymbol{q}_a) = D_{uu}\ddot{q}_u + \boldsymbol{D}_{ua}\ddot{\boldsymbol{q}}_a + C_{uu}\dot{q}_u + \boldsymbol{C}_{ua}\dot{\boldsymbol{q}}_a + G_u, \tag{5}$$

Stability of the unactuated subsystem $\mathcal{S}_u$ given in (4) is related to desired actuated joint $\boldsymbol{q}_a^d$ [7].

Under control (3) with $\ddot{\boldsymbol{q}}_a = \boldsymbol{v}_a^{\text{ext}}$, the BEM is defined as element q_u of the equilibrium for the closed-loop dynamics, that is,

$$\mathcal{E} = \{q_u^e : \Gamma_0(q_u; \boldsymbol{q}_a) = 0\}, \tag{6}$$

where

$$\Gamma_0(q_u; \boldsymbol{q}_a) = \Gamma(q_u; \boldsymbol{q}_a)|_{\dot{q}_u=0, \ddot{q}_u=0}, \tag{7}$$

and $\boldsymbol{C}_{ua}(\dot{\boldsymbol{q}}_a)$ is the term $\boldsymbol{C}_{ua}$ evaluated at $\dot{q}_u = 0$. The expression $\Gamma(q_u; \boldsymbol{q}_a)$ is to account for the dependence on the profile $\boldsymbol{q}_a$ and a similar form is used throughout this paper. As shown in (6), the BEM is an instantaneous equilibrium point under the current control $\boldsymbol{u}$ (and $\boldsymbol{v}_a^{\text{ext}}$). For example, the base link of the rotary inverted pendulum following a constant rotation angle (constant θ) would result in a BEM of a zero angle for the inverted pendulum (i.e., $\alpha = 0$), whereas following a constant acceleration trajectory (constant $\ddot{\theta}$), the BEM is a constant angle of the inverted pendulum (constant α) whose value depends on the base rotational acceleration. The unactuated coordinates are stabilized to the BEM and the control is updated as

$$\boldsymbol{v}_a^{\text{int}} = -\boldsymbol{D}_{ua}^{+}(D_{uu}v_u + C_{uu}\dot{q}_u + \boldsymbol{C}_{ua}\dot{\boldsymbol{q}}_a + G_u), \tag{8}$$

where the superscript "$^+$" denotes the pseudo-inverse operator and v_u is the auxiliary control that drives $q_u \to q_u^e$ exponentially. The design in (3) and (8) is the EIC control [1], [3].

Problem Statement: With the above description of the zero dynamics $\mathcal{S}_0$ and BEM $\mathcal{E}$ for underactuated balance robot, the goal of this work is to build a learning-based approach to estimate and obtain BEM and zero dynamics without knowing the robot dynamic model (1).

III. Main Results

A. Zero Dynamics and BEM

In this subsection, we build the connection between the BEM and the zero dynamics of underactuated balance robot. Solving and analyzing the unactuated coordinate profile q_u of the zero dynamics $\mathcal{S}_0$ is challenging since it is a nonlinear differential equation. Considering the ideal case when the actuated joint $\boldsymbol{q}_a$ follows the desired trajectory $\boldsymbol{q}_a^d$, the BEM can be solved by imposing the condition $\boldsymbol{q}_a = \boldsymbol{q}_a^d$ to (6). The BEM for the desired trajectory becomes

$$\mathcal{E} = \{q_u^e : \Gamma_0(q_u; \boldsymbol{q}_a^d) = 0\}. \tag{9}$$

Instead of solving the nonlinear differential equation (4), we approximate the solution by using the BEM given by (9). We consider the approach given the observation that unactuated joint is moving around the BEM. By recognizing the robot in a quasi-static motion, the BME is the expected trajectory of the unactuated joint to guarantee the system balance. The control can be designed to drive unactuated system following the BEM to guarantee stability [1], [2].

Denoting the solution of $\mathcal{S}_0$ as q_u^d when $\boldsymbol{q}_a$ following $\boldsymbol{q}_a^d$ perfectly, that is $\Gamma(q_u^d; \boldsymbol{q}_a^d) = 0$. We obtain the following results between the BEM q_u^e given by (9) and q_u^d. The proof is given in appendix.

Lemma 1: Given the robot dynamics (1), when $\boldsymbol{q}_a$ following $\boldsymbol{q}_a^d$ perfectly under control (3), the unactuated coordinate is q_u^d and the associated BEM is q_u^e given by (9). The difference between $\Gamma(q_u^d; \boldsymbol{q}_a^d)$ and $\Gamma(q_u^e; \boldsymbol{q}_a^d)$ by (5) is the rate of momentum $H_u = D_{uu}\dot{q}_u^e$, namely,

$$\Delta\Gamma = \Gamma(q_u^e; \boldsymbol{q}_a^d) - \Gamma(q_u^d; \boldsymbol{q}_a^d) = \tfrac{d}{dt}(D_{uu}\dot{q}_u^e) = \dot{H}_u. \tag{10}$$

Moreover, the difference between q_u^d and q_u^e is bounded.

It is not a coincidence that (10) holds. When $\boldsymbol{q}_a \to \boldsymbol{q}_a^d$, the unactuated coordinate q_u moves in a quasi-static mode, which possesses zero angular momentum [1]. Therefore, the difference between $\Gamma(q_u^e; \boldsymbol{q}_a^d)$ and $\Gamma(q_u^d; \boldsymbol{q}_a^d)$ is just the angular momentum change. When the unactuated subsystem converges to a state with constant momentum, i.e., $\Delta\Gamma = \dot{H}_u = 0$, there is no difference of the vector field of zero dynamics under pairs $(\boldsymbol{q}_a^d, q_u^d)$ and $(\boldsymbol{q}_a^d, q_u^e)$. Such a state is commonly observed in underactuated balance robot control. For instance, when tracking a circle with constant velocity, the roll angle of the autonomous bicycle finally converges to a constant and the roll motion possesses zero angular momentum [5]. A similar case is found when a rotary inverted pendulum system moves with a constant angular acceleration of the base link. For those actuated subsystem trajectories, $\Gamma\left(q_u^d; \boldsymbol{q}_a^d\right) = 0$ automatically degenerates to $\Gamma\left(q_u^e; \boldsymbol{q}_a^d\right) = 0$, with $\dot{q}_u^d = 0$ and therefore, $q_u^d = q_u^e$ holds.

B. Learning-Based BEM and Zero Dynamics Estimation

Without knowing the physical model, we use a learning-based data-driven model to estimate the BEM. Note that the BEM is obtained by using the unactuated subsystem dynamics rather than the entire robotic system dynamics. BEM estimation requires function inversion and the learning model should capture the coupling effects between the actuated and unactuated subsystems.

We consider using the GP model to capture the unactuated subsystem dynamics $\mathcal{S}_u$ in (2b) as

$$q_u = f_{GP}(\boldsymbol{x}) + w, \tag{11}$$

where $w \sim \mathcal{N}(0, \Sigma)$ is the zero-mean Gaussian noise with variance Σ, and $\boldsymbol{x} = [\ddot{\boldsymbol{q}}_a^T \ \dot{\boldsymbol{q}}_a^T \ \boldsymbol{q}_a^T \ \ddot{q}_u \ \dot{q}_u]^T \in \mathbb{R}^{3n-1}$ is the dependent variable. The GP model (11) takes q_u as the output, rather than velocity field $\dot{q}_u, \ddot{q}_u$ that is commonly used for dynamic estimation [2], [3]. Denote the training data set as $\mathcal{D} = \{\boldsymbol{X}, \boldsymbol{Y}\} = \{\boldsymbol{x}_i, q_{ui}\}_{i=1}^N$, where $\boldsymbol{X} = \{\boldsymbol{x}_i\}_{i=1}^N$, $\boldsymbol{Y} = \{q_{ui}\}_{i=1}^N$, and $N \in \mathbb{N}$ is the number of the data point. We also use $\boldsymbol{X}, \boldsymbol{Y}$ to represent the matrices composed of all $\boldsymbol{x}_i$ and q_{ui}. The GP model is obtained by maximizing the likelihood function

$$\log(\boldsymbol{Y}; \boldsymbol{X}, \boldsymbol{\theta}) = -\tfrac{1}{2}\boldsymbol{Y}^T\boldsymbol{K}^{-1}\boldsymbol{Y} - \tfrac{1}{2}\log\det(\boldsymbol{K}),$$

where $\boldsymbol{K} = (K_{ij})$, $K_{ij} = k(\boldsymbol{x}_i, \boldsymbol{x}_j) = \sigma_f^2 \exp(-\frac{1}{2}(\boldsymbol{x}_i - \boldsymbol{x}_j)^T\boldsymbol{W}(\boldsymbol{x}_i - \boldsymbol{x}_j)) + \sigma_0^2\delta_{ij}$, $\boldsymbol{W} = \mathrm{diag}\{W_1, \cdots, W_m\} > 0$, $\delta_{ij} = 1$ for $i = j$ only, and $\boldsymbol{\theta} = \{\boldsymbol{W}, \sigma_f, \sigma_0\}$. Given the new measurement data $\boldsymbol{x}^*$, the GP model predicts the mean value and the standard deviation of the unmodeled dynamics

$$\mu(\boldsymbol{x}^*) = \boldsymbol{k}^T\boldsymbol{K}^{-1}\boldsymbol{Y}, \ \Sigma(\boldsymbol{x}^*) = k^* - \boldsymbol{k}^T\boldsymbol{K}^{-1}\boldsymbol{k}, \tag{12}$$

where $\boldsymbol{k} = \boldsymbol{k}(\boldsymbol{x}^*, \boldsymbol{X})$ and $k^* = k(\boldsymbol{x}^*, \boldsymbol{x}^*)$. The unactuated joint motion is then approximated by using prediction $\mu(\boldsymbol{x}^*)$. The GP prediction error is bounded by the following Lemma.

Lemma 2 ([21, Theorem 6]): Given the training dataset $\mathcal{D}$, if the kernel function $k(\boldsymbol{x}_i, \boldsymbol{x}_j)$ is chosen such that q_u has a finite reproducing kernel Hilbert space norm $\|q_u\|_k < \infty$, for given $0 < \eta < 1$,

$$\Pr\{\|q_u - \mu(\boldsymbol{x})\| \le \|\Sigma^{\frac{1}{2}}(\boldsymbol{x})\kappa\|\} \ge \eta, \tag{13}$$

where $\Pr\{\cdot\}$ denotes the probability of an event, $\eta \in (0, 1)$, $\kappa = \sqrt{2|q_u|_k^2 + 300\varsigma \ln^3 \frac{N}{1-\eta^{\frac{1}{m}}}}$, $\varsigma = \max_{\boldsymbol{x}, \boldsymbol{x}' \in \boldsymbol{X}} \frac{1}{2}\ln|1 + \sigma^{-2}k(\boldsymbol{x}, \boldsymbol{x}')|$.

With known physical robot dynamics, the BEM is obtained by inversion, that is, $q_u^e = \Gamma^{-1}(\boldsymbol{q}_a)$ and estimation of the BEM from the GP model (11) does not need to take inversion. The instantaneous BEM (depending on $\ddot{\boldsymbol{q}}_a$) is computed as reference by enforcing $\dot{q}_u = \ddot{q}_u = 0$, that is,

$$\mathcal{E}_l = \{q_u^e : q_u^e = \mu(\boldsymbol{x}_0^e)\}, \ \boldsymbol{x}_0^e = \{\ddot{\boldsymbol{q}}_a, \dot{\boldsymbol{q}}_a, \boldsymbol{q}_a, 0, 0\}. \tag{14}$$

The learning-based BEM estimate $\mathcal{E}_l$ can be evaluated in real time. Using the results in Lemma 1 and (15), we obtain that for given trajectory $\boldsymbol{q}_a^d$

$$\Pr\{\|q_u^d - \mu(\boldsymbol{x}_0^e)\| \leq \|\Sigma^{\frac{1}{2}}(\boldsymbol{x}_0^e)\kappa\| + \tfrac{\Delta\Gamma_{\max}}{F_{\min}}\} \geq \eta, \quad (15)$$

where $\boldsymbol{x}_0^e = \{\ddot{\boldsymbol{q}}_a^d, \dot{\boldsymbol{q}}_a^d, \boldsymbol{q}_a^d, 0, 0\}$ and $\Delta\Gamma_{\max}$ and $F_{\min}$ are given in appendix.

C. BEM and GPDM

We further investigate the relationship between learned BEM and the zero dynamics. For underactuated balance robots with a large number of DOFs, a learning-based dimensionality-reduction model such as GPDM is an effective method to obtain the robot dynamics.

GPDM is a nonlinear dimensionality reduction method to obtain the motion dynamics in a latent space. We build a GPDM for underactuated balance robots. We denote the latent state variable as χ and here we assume $\chi \in \mathbb{R}$ for one-dimensional zero dynamics. The latent dynamics $\mathcal{S}_l$ are based on the GPDM [18], [22] as

$$\mathcal{S}_l: \ \dot{\chi} = f(\chi, \boldsymbol{\alpha}) + w_f, \ \boldsymbol{q} = \boldsymbol{g}(\chi, \boldsymbol{\beta}) + \boldsymbol{w}_g, \quad (16)$$

where $\boldsymbol{\alpha}$ and $\boldsymbol{\beta}$ are hyperparameter vectors, and w_f and $\boldsymbol{w}_g$ are zero-mean Gaussian noises. In latent dynamics $\mathcal{S}_l$, $f(\chi, \boldsymbol{\alpha})$ builds the dynamics relationship in latent space, while GP model $\boldsymbol{g}(\chi, \boldsymbol{\beta})$ maps from the latent space to the high-dimension joint space. The Gaussian kernel is used in those GP models. Solving the hyperparameters and latent variables is equivalent to maximizing the posterior probability distribution

$$\max_{\mathcal{X}, \boldsymbol{\alpha}, \boldsymbol{\beta}} p(\mathcal{X}, \boldsymbol{\alpha}, \boldsymbol{\beta} | \mathcal{Q}), \quad (17)$$

where $\mathcal{X} = \{\chi_i\}$ is the corresponding latent data set for high-dimension data set $\mathcal{Q} = \{\boldsymbol{q}_i\}$.

In [18], the relationship between the zero dynamics and GPDM-based latent model was established. The GPDM model is proven to be equivalent to zero dynamics under a coordinate transformation and perfectly tracking conditions. The maximization problem is converted as a minimization problem by taking the negative logarithm. Moreover, (17) was modified as the following

$$\min_{\mathcal{X}, \boldsymbol{\alpha}, \boldsymbol{\beta}, \boldsymbol{c}} -\log p(\mathcal{Q}|\mathcal{X}, \boldsymbol{\beta}) - \log p(\mathcal{X}|\boldsymbol{a}lpha) + \|\mathcal{X} - \boldsymbol{c}\mathcal{Q}\|^2.$$

In solving the above optimization problem, we enforce $\chi = \boldsymbol{c}\boldsymbol{q}$ (and then $\mathcal{X} = \boldsymbol{c}\mathcal{Q}$), where the vector $\boldsymbol{c}^T \in \mathbb{R}^n$ is used to capture the desired out trajectory for (1). For example, for bipedal robots, it is commonly defined $\vartheta = \boldsymbol{c}\boldsymbol{q}$ as gait phase variable, and the desired output is then obtained as $\boldsymbol{y}_d = \boldsymbol{q}_a - \boldsymbol{q}_a^d = \boldsymbol{q}_a - \boldsymbol{h}(\vartheta) = \boldsymbol{0}$, where function $\boldsymbol{h}(\cdot)$ is obtained by a Bézier polynomial. The output $\boldsymbol{y}_d = \boldsymbol{0}$ then serves as a virtual holonomic constraint connecting the actuated and unactuated joints [11], [12].

We approximate the unactuated coordinate $q_u^d \approx q_u^e \approx \mu(\boldsymbol{x}_0^e)$. Meanwhile, from the latent dynamics S_l, we obtain the parameter $\boldsymbol{c}$ and investigate the relationship between the BEM and zero dynamics in the latent space. Considering the following form $\hat{\chi} = \boldsymbol{c}[\boldsymbol{q}_a^T \ \mu(\boldsymbol{x}_0^e)]^T$, we re-construct the latent variable using the BEM to replace the q_u^d. The difference $\chi - \hat{\chi}$ further informs the error between BEM and zero dynamics.

To illustrate the application of the above-revealed relationship between the BEM and the zero dynamics, we consider the bipedal robot control. One of the challenges in bipedal walker control is to construct the desired gait profile [7]. We can use machine learning techniques to construct the gait profile. Considering using a human subject's gait profile to construct a gait profile for the bipedal robot, a learning-based model (14) is trained to obtain the BEM estimation $\mu(\boldsymbol{x}_0^e)$ for the bipedal robot. We then obtain the gait parameter $\boldsymbol{c}$ for human walking gait data and construct the latent variable $\hat{\chi}$ (similar to gait phase variable ϑ) using the GPDM. Comparing χ and $\hat{\chi}$, we evaluate the gait pattern estimation performance in latent space and further modify the gait profile for the bipedal robot. We will illustrate and demonstrate examples in the next section.

IV. Experiments

In this section, we present the experimental results using the rotary inverted pendulum and the bipedal robot walker to illustrate and validate the proposed analysis.

A. Rotary Pendulum Example

We first use the rotary inverted pendulum to illustrate the analysis. Fig. 1(a) shows the 2-DOF rotary inverted pendulum in experiments. The base joint θ is actuated by a DC motor and the inverted pendulum joint α is unactuated. For α, the zero position is vertically upwards. The dynamics model for the rotary pendulum is expressed in the form of (1) with $q_a = \theta$ and $q_u = \alpha$. The model parameters are $\boldsymbol{B} = [1 \ 0]^T$, matrix $\boldsymbol{D}$ and $\boldsymbol{H} = [h_a \ h_u]^T = \boldsymbol{C}(\boldsymbol{q}, \dot{\boldsymbol{q}})\dot{\boldsymbol{q}} + \boldsymbol{G}(\boldsymbol{q})$ have the elements

$$\begin{aligned}
D_{aa} &= C(m_p l_r^2 + 0.25 m_p l_p^2 \, \mathrm{s}_{q_u}^2 + J_r), \\
D_{au} &= -0.5 C m_p l_p l_r \, \mathrm{c}_{q_u}, \ D_{uu} = C(J_p + 0.25 m_p l_p^2), \\
h_a &= C(0.5 m_p l_p^2 \dot{q}_a \dot{q}_u \, \mathrm{s}_{q_u} \, \mathrm{c}_{q_u} + 0.5 m_p l_p l_r \dot{q}_u^2 \, \mathrm{s}_{q_u} + \\
&\quad d_r \dot{q}_a + k_g^2 k_t k_m \dot{q}_a / R_m) + K_g k_t \dot{q}_u, \\
h_u &= C(d_p \dot{q}_u - 0.25 m_p l_p^2 \, \mathrm{c}_{q_u} \, \mathrm{s}_{q_u} \, \dot{q}_a^2 - 0.5 m_p l_p g \, \mathrm{s}_{q_u}),
\end{aligned}$$

where $\mathrm{s}_x := \sin x$ and $\mathrm{c}_x := \cos x$ for angle x, l_r, J_r and d_r are the length, mass inertia and viscous damping coefficient of the base link, l_p, J_p and d_p are corresponding parameters of the pendulum, m_p is the pendulum mass, g is the gravitational constant, and C is a constant. The values of these parameters can be found in [23]. The control input is the applied DC voltage, $u = V_m$. The control implementation was at 400 Hz in Matlab/Simulink with Quanser's hardware-in-the-loop real-time system.

The training data are obtained by using a controller to excite the system. The controller is $u = \boldsymbol{k}^T \boldsymbol{e}$, where $\boldsymbol{k} = [2 \ 2 \ -10 \ 10]^T$ and $\boldsymbol{e} = [\theta - \theta_t \ \ \alpha \ \ \dot{\theta} - \dot{\theta}_t \ \ \dot{\alpha}]^T$ and θ_t is the combination of sine waves with different amplitudes and frequencies for training data collection. The control parameter $\boldsymbol{k}$ is selected arbitrarily without the need

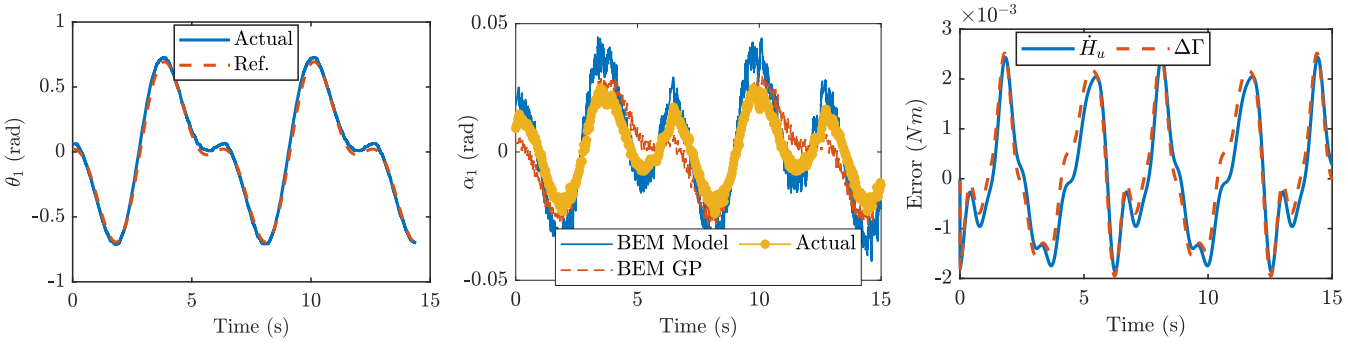

(a) (b) (c)

Fig. 2. Example results of the rotary pendulum motion. (a) Rotary arm angle θ. (b) Pendulum link angle α. (c) Comparison of the zero dynamics estimation difference $\Delta\Gamma$.

to guarantee stability and performance. The actual trajectory of the pendulum did not follow the reference. We trained a GP regression model (14) to estimate the BEM and a total of 500 training data points were randomly selected from a large dataset including unsuccessful balancing trails.

Fig. 2 shows the experimental results. Fig. 2(a) shows the base link joint θ tracking performance with the reference trajectory θ_d. We chose the reference trajectory as a composite sinusoidal curve [2]. Fig. 2(b) shows the inverted pendulum joint α profile. The GP-predicted BEM and the model-based calculation demonstrate a similar trend and the pendulum joint follows the BEM closely. The angular measurements were sampled at high frequency and a numerical derivative was used for control design, which resulted in noisy signals in the GP-based BEM prediction as shown in the figure. To illustrate and validate the result in Lemma 1, we first note that the output θ perfectly follows the given trajectory θ_d. Fig. 2(c) further shows the rate of angular momentum change $\dot{H}_u(\alpha)$ and the GP-based prediction of $\Delta\Gamma$. Both curves follow the same trend closely. The error between them is due to both the measurement (and its numerical derivatives) and GP prediction errors.

B. Bipedal Walker Gait Design

Fig. 1(b) shows the experimental platform of the bipedal walker that was fabricated and used in the experiments. The robot has five links (i.e., 5 DOFs) and the torso joint is unactuated. Fig.3(a) shows the schematics of the robotic walker. Table I shows the values of the model parameters such as the lengths and the masses of the base link (i.e., the torso), thigh links, and shank links that are labeled with subscripts "b", "t", and "s", respectively. The analytical model can be found in [24]. The experiment was conducted at 115 Hz real-time control frequency. For the bipedal robot, $q_u = q_1$ and $\boldsymbol{q}_a = [q_2\ q_3\ q_4\ q_5]^T$.

TABLE I

PHYSICAL PARAMETERS OF THE BIPEDAL ROBOT

L_b(m)	L_t(m)	L_s(m)	m_b (kg)	m_t(kg)	m_s(kg)
0.025	0.2	0.22	3.60	1.07	0.19

We first show the bipedal robot control experiment results. Fig. 4 shows the gait profile results. The hip and knee angles

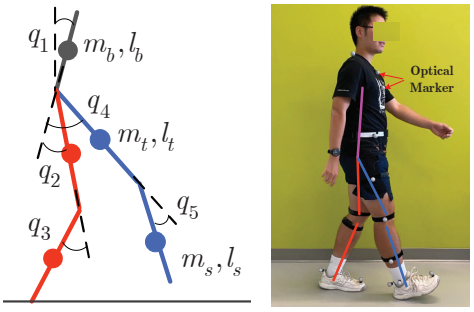

(a) (b)

Fig. 3. (a) Schematic of the 5-link bipedal robotic walker. (b) Human walking experiments to collect gait profile data.

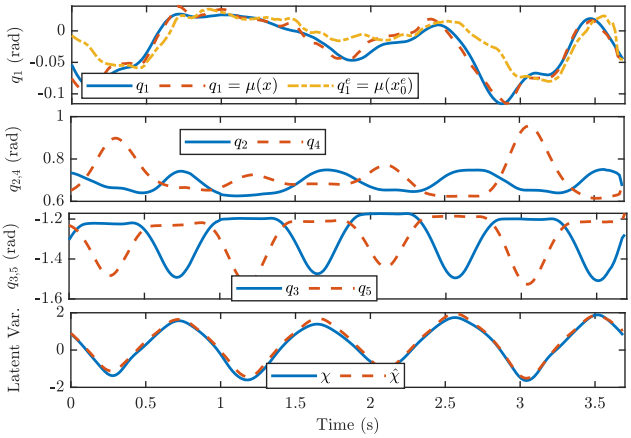

Fig. 4. Bipedal robot walking experiments. From the upper to lower plots: torso angle q_1, hip angles q_2 and q_4, knee angles q_3 and q_5, and the latent variable χ and its estimate $\hat{\chi}$.

display a repeated pattern. While the torso angle maintains a small oscillation around the vertical position. Using the experiment data, we trained the GPDM latent dynamics $\mathcal{S}_l$ and used a GP model to estimate the BEM. The top plot of Fig. 4 shows the GP prediction of the torso joint angle q_1 and the corresponding BEM, that is, q_1^e. The actual joint q_1 follows the profile of q_1^e except large difference at $t = 0.2$ s and $t = 3$ s. This is due to the hip angles (q_2 and q_4) having a large variation from the previous step as shown in the figure. The gait parameter vector $\boldsymbol{c}$ of the robot's current gait is obtained as $\boldsymbol{c} = [-0.82\ 0.97\ -0.72\ -4.09\ 5.91]$ in the GPDM estimation. As shown in the bottom plot in the figure, we re-constructed the latent variable using the BEM prediction. Since q_1 is close to q_1^e, $\hat{\chi}$ closely follows χ.

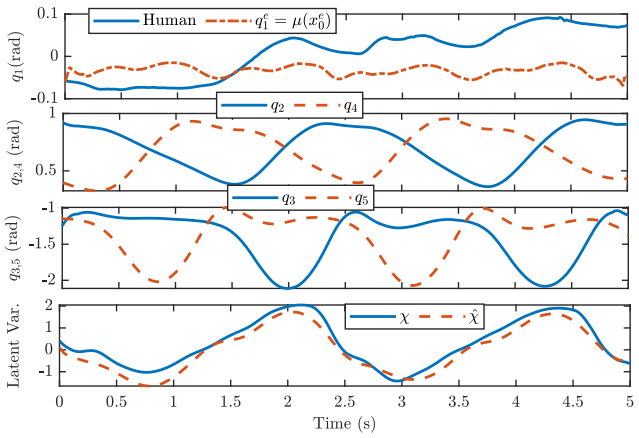

Fig. 5. Learning human gait to construct bipedal robot gait profile. From the upper to lower plots: trunk, hip, and knee angles, and the latent variable χ and its estimate $\hat{\chi}$. Human joint angles are defined in the same manner as the bipedal robot shown in Fig. 1(b).

We next demonstrate the application of transferring a human gait profile to the robotic walker. Since the torso joint of the robotic walker is unactuated, not all human-demonstrated gait can be transferred to the bipedal robot. We can use the BEM estimation as a criterion to validate the robotic walker's torso motion. Meanwhile, the bipedal robot and human subjects have different mass distributions and link lengths. We first apply a linear transformation to modify the human demonstrated gait so that the joint angle range satisfies the bipedal walker physical constraint. Fig. 3(b) shows the human walking experiment to collect human gait profiles. A motion capture system was used to obtain human gait profiles. Fig. 5 shows the hip and knee angles of human walking gait. From the human gait profile, we obtained the gait parameter vector $\boldsymbol{c} = [-1.47\ 1.75\ 1.86\ -1.75\ 1.95]$ by the GPDM estimation. We tried to use the human gait profile to create the desired gait for the robotic walker and therefore, we obtained the estimated BEM $\mu(\boldsymbol{x}_0^e)$. When the bipedal robot followed the human gait $\boldsymbol{y} = \boldsymbol{q}_a - \boldsymbol{q}_a^d = \boldsymbol{0}$, the torso displays a stable and periodic motion response around -0.05 rad as shown in the top plot of Fig. 5, whereas the latent variable of the robot $\hat{\chi}$ followed the human gait pattern χ closely. The human-inspired gait can be further used as the targeted gait profile and vector $\boldsymbol{c}$ can be used to capture the progress of each step to design the gait controller.

V. Conclusion

We presented a learning-based approach to obtain the balance manifold profile estimation and its relationship with the zero dynamics for underactuated balance robots. Based on the analytical model, we first showed that the balance manifold is an accurate estimate of the equilibria of the zero dynamics. To extend the results when robot dynamics are unavailable, we built a GP regression model to estimate the balance manifold. The estimation of the balance manifold was further extended to the GPDM, which was proven equivalent to the zero dynamics. The use of the learning-based balance manifold estimation was demonstrated for both robot control and desired trajectory design. The analysis was illustrated experimentally through a rotary inverted pendulum control and a human-inspired gait design for a bipedal robot.

Appendix

Proof of Lemma 1

Proof: When $\boldsymbol{q}_a$ perfectly follows $\boldsymbol{q}_a^d$, $(\boldsymbol{q}_a^d, q_u^d)$ satisfies zero dynamics (4) and therefore, we obtain $\Gamma(q_u^d; \boldsymbol{q}_a^d) = 0$. Thus, we need to show that $\Delta\Gamma = \dot{H}_u(q_u^e)$. Noting that $\Gamma(q_u^e; \boldsymbol{q}_a^d) = 0$, plugging this relationship into (10) results in

$$\begin{aligned}\Delta\Gamma &= D_u\ddot{q}_u^e + \boldsymbol{D}_{ua}\ddot{\boldsymbol{q}}_a^d + \boldsymbol{C}_{ua}\dot{\boldsymbol{q}}_a^d + C_{uu}\dot{q}_u^e + G_u \\ &= \Gamma(\boldsymbol{q}_a^d, q_u^e) + D_u\ddot{q}_u^e + \boldsymbol{C}_{ua}(\dot{q}_u^e)\dot{\boldsymbol{q}}_a^d + C_{uu}\dot{q}_u^e \\ &= D_u\ddot{q}_u^e + \boldsymbol{C}_{ua}(\dot{q}_u^e)\dot{\boldsymbol{q}}_a^d + C_{uu}\dot{q}_u^e, \end{aligned} \tag{18}$$

where $\boldsymbol{C}_{ua}(\dot{q}_u^e) = \boldsymbol{C}_{ua} - \boldsymbol{C}_{ua}(\dot{\boldsymbol{q}}_a^d)$ denotes the items containing $\dot{q}_u^e$.

Noting that $C_{nj} = \sum_{k=1}^{n} c_{njk}\dot{q}_k$, $j = 1, \cdots, n-1$, we collect the terms related with $\dot{q}_u^e$, that is, $k = n$, and obtain

$$c_{njn} = \tfrac{1}{2}\left(\tfrac{\partial D_{nj}}{\partial q_n} + \tfrac{\partial D_{nn}}{\partial q_j} - \tfrac{\partial D_{jn}}{\partial q_n}\right) = \tfrac{1}{2}\tfrac{\partial D_{uu}}{\partial q_j},$$

where symmetric property $D_{nj} = D_{jn}$ is used. Therefore, each element in matrix $\boldsymbol{C}_{ua}$ is expressed as

$$C_{nj} = \tfrac{1}{2}\tfrac{\partial D_{nn}}{\partial q_j}\dot{q}_n + \tfrac{1}{2}\sum_{k=1}^{n-1} c_{njk}\dot{q}_k, j = 1, \cdots, n-1.$$

The explicit forms of $\boldsymbol{C}_{ua}(\dot{q}_u^e)$ and $\boldsymbol{C}_{ua}(\dot{\boldsymbol{q}}_a^d)$ become

$$\boldsymbol{C}_{ua}(\dot{q}_u^e) = \left(\tfrac{1}{2}\tfrac{\partial D_{nn}}{\partial q_j}\dot{q}_u^e\right), \boldsymbol{C}_{ua}(\dot{\boldsymbol{q}}_a^d) = \left(\tfrac{1}{2}\sum_{k=1}^{n-1} c_{njk}\dot{q}_k\right)$$

for $j = 1, \cdots, n-1$. Similarly we obtain that $C_{uu} = C_{nn} = \frac{1}{2}\sum_{k=1}^{n}\frac{\partial D_{nn}}{\partial q_k}\dot{q}_k$. Given above relationships, (18) becomes

$$\begin{aligned}\Delta\Gamma &= D_{uu}\ddot{q}_u^e + \tfrac{1}{2}\sum_{j=1}^{n-1}\tfrac{\partial D_{nn}}{\partial q_j}\dot{q}_u^e\dot{q}_j + \tfrac{1}{2}\sum_{k=1}^{n}\tfrac{\partial D_{nn}}{\partial q_k}\dot{q}_k\dot{q}_u^e \\ &= D_{uu}\ddot{q}_u^e + \dot{D}_{uu}\dot{q}_u^e = \tfrac{d}{dt}(D_{uu}\dot{q}_u^e) = \dot{H}_u, \end{aligned} \tag{19}$$

where momentum $H_u = D_{uu}\dot{q}_u^e$. In the last two steps in (19), we use the fact that $\frac{1}{2}\sum_{j=1}^{n-1}\frac{\partial D_{nn}}{\partial q_j}\dot{q}_j = \frac{1}{2}\sum_{j=1}^{n}\frac{\partial D_{nn}}{\partial q_j}\dot{q}_j$ and $q_n = q_u^e$.

Defining $H_u(q_u^e)$ as the angular momentum of the unactuated subsystem, from (19), we obtain

$$H_u(q_u^e) = \int_0^t \Delta\Gamma d\tau = D_{uu}\dot{q}_u^e. \tag{20}$$

Because the profile $\boldsymbol{q}_a^d$ is bounded, the BEM q_u^e and $\dot{q}_u^e$ are bounded, that is, $|\dot{q}_u^e| \le v_{u,\max}^e$ with finite $v_{u,\max}^e > 0$. Let $D_{uu,\max}$ be the upper bound D_{uu}, and for H_u, we have

$$|H_u(q_u^e)| = |D_{uu}\dot{q}_u^e| \le H_{u,\max} := D_{uu,\max}v_{u,\max}^e.$$

Expanding $\Gamma(\boldsymbol{q}_u^d; \boldsymbol{q}_a^d)$ around the profile $\boldsymbol{p}_u^e = [q_u^e\ \dot{q}_u^e\ \ddot{q}_u^e]^T$ and neglecting the higher order terms, we have

$$\Delta\Gamma = \tfrac{\partial\Gamma(\boldsymbol{q}_u^d;\boldsymbol{q}_a^d)}{\partial\boldsymbol{p}_u^d}\big|_{\boldsymbol{p}_u^d=\boldsymbol{p}_u^e}(\boldsymbol{p}_u^d - \boldsymbol{p}_u^e) := \boldsymbol{F}(\boldsymbol{p}_u^d - \boldsymbol{p}_u^e) \tag{21}$$

where $\boldsymbol{p}_u^d = [q_u^d\ \dot{q}_u^d\ \ddot{q}_u^d]^T$. The boundedness of the angular momentum H_u indicates the boundedness of $\Delta\Gamma$ and same for the difference between the profile $\boldsymbol{p}_u^d$ and $\boldsymbol{p}_u^e$. Thus we obtain $|\boldsymbol{p}_u^e - \boldsymbol{p}_u^d| \le \frac{\Delta\Gamma_{\max}}{F_{\min}}$, where $F_{\min} = \inf_{\boldsymbol{p}_u^e}\|\boldsymbol{F}\| > 0$ and $\Delta\Gamma_{\max} > |\Delta\Gamma|$ is the upper bound. This completes the proof. ■

REFERENCES

[1] N. Getz, "Dynamic inversion of nonlinear maps with applications to nonlinear control and robotics," Ph.D. dissertation, Dept. Electr. Eng. and Comp. Sci., Univ. Calif., Berkeley, CA, 1995.

[2] F. Han and J. Yi, "Stable learning-based tracking control of underactuated balance robots," *IEEE Robot. Automat. Lett.*, vol. 6, no. 2, pp. 1543–1550, 2021.

[3] K. Chen, J. Yi, and D. Song, "Gaussian processes model-based control of underactuated balance robots," *IEEE Trans. Robotics*, vol. 39, no. 1, pp. 572–589, 2023.

[4] P. Wang, J. Yi, T. Liu, and Y. Zhang, "Trajectory tracking and balance control of an autonomous bikebot," in *Proc. IEEE Int. Conf. Robot. Autom.*, Singapore, 2017, pp. 2414–2419.

[5] F. Han, X. Huang, Z. Wang, J. Yi, and T. Liu, "Autonomous bikebot control for crossing obstacles with assistive leg impulsive actuation," *IEEE/ASME Trans. Mechatronics*, vol. 27, no. 4, pp. 1882–1890, 2022.

[6] J. Grizzle, M. Di Benedetto, and F. Lamnabhi-Lagarrigue, "Necessary conditions for asymptotic tracking in nonlinear systems," *IEEE Trans. Automat. Contr.*, vol. 39, no. 9, pp. 1782–1794, 1994.

[7] E. R. Westervelt, J. W. Grizzle, and D. E. Koditschek, "Hybrid zero dynamics of planar biped walkers," *IEEE Trans. Automat. Contr.*, vol. 48, no. 1, pp. 42–56, 2003.

[8] M. Mihalec and J. Yi, "Capturability of inverted pendulum gait model under slip conditions," in *Proc. ASME Dyn. Syst. Control Conf.*, Atlanta, GA, 2018, article DSCC2018-9203.

[9] K. Chen, Y. Zhang, J. Yi, and T. Liu, "An integrated physical-learning model of physical human-robot interactions with application to pose estimation in bikebot riding," *Int. J. Robot. Res.*, vol. 35, no. 12, pp. 1459–1476, 2016.

[10] M. Maggiore and L. Consolini, "Virtual holonomic constraints for euler–lagrange systems," *IEEE Trans. Automat. Contr.*, vol. 58, no. 4, pp. 1001–1008, 2013.

[11] N. Kant and R. Mukherjee, "Orbital stabilization of underactuated systems using virtual holonomic constraints and impulse controlled poincaré maps," *Syst. Contr. Lett.*, vol. 146, pp. 1–9, 2020, article 104813.

[12] A. Mohammadi, M. Maggiore, and L. Consolini, "Dynamic virtual holonomic constraints for stabilization of closed orbits in underactuated mechanical systems," *Automatica*, vol. 94, pp. 112–124, 2018.

[13] C. Chevallereau, E. R. Westervelt, and J. W. Grizzle, "Asymptotically stable running for a five-link, four-actuator, planar bipedal robot," *Int. J. Robot. Res.*, vol. 24, no. 6, pp. 431–464, 2005.

[14] A. Goo, C. A. Laubscher, and J. T. Sawicki, "Hybrid Zero Dynamics Control of an Underactuated Lower-Limb Exoskeleton for Gait Guidance," *ASME J. Dyn. Syst., Meas., Control*, vol. 144, no. 6, 03 2022, 061008.

[15] K. Chen, M. Trkov, and J. Yi, "Hybrid zero dynamics of human walking with foot slip," in *Proc. Amer. Control Conf.*, Seattle, WA, 2017, pp. 2124–2129.

[16] D. Nguyen-Tuong and J. Peters, "Model learning for robot control: A survey," *Cogn. Process*, vol. 12, pp. 319–340, 2011.

[17] T. Beckers, D. Kulić, and S. Hirche, "Stable Gaussian process based tracking control of Euler–Lagrange systems," *Automatica*, vol. 103, pp. 390–397, 2019.

[18] K. Chen and J. Yi, "On the relationship between manifold learning latent dynamics and zero dynamics for human bipedal walking," in *Proc. IEEE/RSJ Int. Conf. Intell. Robot. Syst.*, Hamburg, Germany, 2015, pp. 971–976.

[19] N. Kant and R. Mukherjee, "Impulsive dynamics and control of the inertia-wheel pendulum," *IEEE Robot. Automat. Lett.*, vol. 3, no. 4, pp. 3208–3215, 2018.

[20] M. W. Spong, S. Hutchinson, and M. Vidyasagar, *Robot Modeling and Control*. New York, NY: John Wiley & Sons, Inc., 2006.

[21] N. Srinivas, A. Krause, S. M. Kakade, and M. W. Seeger, "Information-theoretic regret bounds for gaussian process optimization in the bandit setting," *IEEE Trans. Inform. Theory*, vol. 58, no. 5, pp. 3250–3265, 2012.

[22] J. M. Wang, D. J. Fleet, and A. Hertmann, "Gaussian process dynamical models for human motion," *IEEE Trans. Pattern Anal. Machine Intell.*, vol. 30, no. 2, pp. 283–298, 2008.

[23] J. Apkarian, P. Karam, and M. Levis, *Instructor Workbook: Inverted Pendulum Experiment for Matlab/Simulink Users*, Quanser Inc., Markham, Ontario, Canada, 2011.

[24] M. Mihalec, "Balance recoverability and control of bipedal robotic walkers with foot slip," Ph.D. dissertation, Dept. Mech. Aero. Eng., Rutgers Univ., Piscataway, NJ, 2022.